Nanoscale Advances

ROYAL SOCIETY OF CHEMISTRY

PAPER

View Article Online
View Journal | View Issue

Cite this: *Nanoscale Adv.*, 2022, **4**, 2468

Bottom-up synthesis of 2D layered high-entropy transition metal hydroxides†

Fei Li, *[a] Shi-Kuan Sun,[b] Yinjuan Chen,[c] Takashi Naka,[d] Takeshi Hashishin,[e] Jun Maruyama [f] and Hiroya Abe*[a]

Low-dimensional high-entropy materials, such as nanoparticles and two-dimensional (2D) layers, have great potential for catalysis and energy applications. However, it is still challenging to synthesize 2D layered high-entropy materials through a bottom-up soft chemistry method, due to the difficulty of mixing and assembling multiple elements in 2D layers. Here, we report a simple polyol process for the synthesis of a series of 2D layered high-entropy transition metal (Co, Cr, Fe, Mn, Ni, and Zn) hydroxides (HEHs), involving the hydrolysis and inorganic polymerization of metal-containing species in ethylene glycol media. The as-synthesized HEHs demonstrate 2D layered structures with interlayer distances ranging from 0.860 to 0.987 nm and homogeneous elemental distribution of designed equimolar stoichiometry in the layers. These 2D HEHs exhibit a low overpotential of 275 mV at 10 mA cm^{-2} in a 0.1 M KOH electrolyte for the oxygen evolution reaction. Superparamagnetic spinel-type high-entropy nanoparticles can also be obtained by annealing these HEHs. Our polyol approach creates opportunities for synthesizing low-dimensional high-entropy materials with promising properties and applications.

Received 17th December 2021
Accepted 20th April 2022

DOI: 10.1039/d1na00871d

rsc.li/nanoscale-advances

Introduction

The concept of high entropy, creating materials by alloying five or more elements in equimolar or near equimolar ratios, was established by the pioneering work of Yeh and Cantor on alloys in 2004,[1,2] and has been extended beyond alloys into the entire materials community since 2015.[3–12] High-entropy materials (HEMs) including alloys,[4] oxides,[13–15] carbides,[16–18] borides,[19–21] nitrides,[22] fluorites,[23] silicides,[9,24] *etc.*, open a vast compositional space for materials design and property optimization. The high configurational entropy of the multi-element system would overcome enthalpic contribution to the total free energy and stabilize multiple elements in a simple single-phase solid solution.[4–6] Unique properties would appear due to the multi-element synergistic effect, abundant defects, *etc.*[7] Powder metallurgy is the most commonly used method to alloy multiple elements.[4,5,25] However, bulk and micron-sized powders are usually obtained because of migration and aggregation of particles at high temperatures.[7,14] Wet-chemistry approaches[22,26–29] and thermal shock approaches[30,31] are developed to synthesize high-entropy nanoparticles. Moreover, the stoichiometry of HEMs obtained from wet-chemistry approaches may deviate from their original design due to the difference in the solubility product constant of the cations.[32–36] Bulk HEMs (*e.g.*, alloys and ceramics) demonstrate exceptional mechanical properties and thermal insulation, while nano-HEMs present promising functional properties for catalysis, Li-ion battery applications, *etc.*[4–7] For example, Reece *et al.* reported enhanced hardness over 40 GPa in high-entropy carbides due to the random interactions between elements at a dislocation core.[16] Hu *et al.* reported that denary oxide nanoparticles demonstrate excellent catalytic performance and superior thermal stability for methane combustion, due to entropy stabilization and more oxygen defects in their materials.[14]

Two-dimensional (2D) materials have received increasing attention since the discovery of graphene.[37–39] Great efforts have been dedicated to exploring new 2D materials due to their unique set of properties and broad applications.[40,41] Unlike the large numbers of research studies on zero-dimensional (nanoparticle) and bulk HEMs, little attention is paid to 2D HEMs. Only limited studies have been reported on 2D HEMs, including high-entropy hydroxides (HEHs),[42] HE oxides,[43] HE carbides,[44,45] HE dichalcogenides,[46] HE halides,[46] and HE phosphorus trisulfides.[46,47] Like the synthesis of other 2D materials, the methods for making 2D HEMs can be divided into two

[a]*Joining and Welding Research Institute, Osaka University, Osaka 5670047, Japan. E-mail: feili@jwri.osaka-u.ac.jp; h-abe@jwri.osaka-u.ac.jp*

[b]*School of Material Science and Energy Engineering, Foshan University, Foshan, 528000, China*

[c]*Key Laboratory of Precise Synthesis of Functional Molecules of Zhejiang Province, School of Science, Instrumentation and Service Center for Molecular Sciences, Westlake University, Hangzhou 310024, China*

[d]*National Institute for Materials Science, Ibaraki 3050047, Japan*

[e]*Faculty of Advanced Science and Technology, Kumamoto University, Kumamoto, 8608555, Japan*

[f]*Osaka Research Institute of Industrial Science and Technology, Osaka 5368553, Japan*

† Electronic supplementary information (ESI) available. See https://doi.org/10.1039/d1na00871d

categories, *i.e.*, top-down and bottom-up.[39] The top-down process starts with the synthesis of bulk HEMs as precursors, followed by exfoliation or etching for thinning them. Hosono *et al.* developed a mechanical exfoliation method to synthesize a series of high-entropy van der Waals 2D materials (dichalcogenides, halides, and phosphorus trisulfides) with an intriguing set of properties.[46] Wang *et al.* developed high-entropy layered double hydroxides (HE-LDH) (FeAlCrCoNiZnCu)–OH intercalated with CO_3^{2-} by a hydrothermal method and exfoliated them to ultrathin defective nanosheets with a diameter of 50 nm with argon plasma.[42] Wang *et al.* also reported the synthesis of spinel-type high-entropy oxide $(FeCrCoNiCu)_3O_4$ nanosheets with diameters up to 100 nm by oxygen plasma exfoliation of HE-LDH.[43] These plasma-exfoliated HE-LDH nanosheets demonstrated efficient electrochemical catalytic activity, such as in the oxygen evolution reaction (OER). Very recently, high-entropy 2D transition metal carbides (MXenes) were achieved through selective etching of Al layers from high-entropy MAX phases by Anasori *et al.* and almost at the same time by Yang *et al.*[44,45] These high-entropy MXenes indicate promising applications including energy storage and catalysis related areas. It is worth noting that the stoichiometry of 2D HEMs may deviate from their original design due to the post-chemical exfoliation and etching.[45] The bottom-up process starts with atomic ingredients and they were assembled together to form 2D HEMs. Miura *et al.* reported a hydrothermal synthesis of CO_3^{2-} intercalated HE layered hydroxide (MgAlCoNiZn)–OH using water as solvent, showing aggregated hexagonal platelet crystals of 300 nm in size.[48] Ting *et al.* reported HE (CoCrFeMnNi)-glycerate for a high performance OER by a solvothermal technique using glycerol as solvent.[49] The HE glycerate has a layered lattice structure and yet a spherical morphology.[49] Due to the difficulty in mixing multiple elements at the nanoscale and almost at the same time forming and maintaining the 2D morphology, it is significantly challenging to synthesize 2D HEMs through a bottom-up process.

In this work, we present an attempt to synthesize 2D layered HEHs through a bottom-up polyol approach. The polyol process is widely recognized as a unique soft chemistry method for the preparation of various low-dimensional materials.[50,51] Six transition metal cations (Co, Cr, Fe, Mn, Ni, and Zn) were selected to give out six five-element and one six-element equimolar high-entropy compositions. A solvothermal treatment using ethylene glycol as solvent was carried out at 200 °C for only 2 h, involving the complexation of polyol with metal cations, hydrolysis and inorganic polymerization. 2D layered HEHs with a large area, high compositional homogeneity, and designed stoichiometry were successfully synthesized. Binary transition metal hydroxides (*e.g.* NiFe, CoNi, and ZnCo) are widely studied as electrocatalysts for water oxidation.[52,53] Doping with additional metal elements in these binary hydroxides, which could tune their surface chemistry and electronic structure, has been used to tailor their OER performance. The combination of multiple 3d transition metal ions in the 2D layered HEHs would possibly tune the activity for the OER. Upon post-annealing at 200 °C, these 2D HEHs could be converted into spinel-type oxide nanoparticles. The corresponding HE spinels contain multiple 3d magnetic ions. It would be of interest if the HE multicomponent spinels have emergent phenomena by an order-by-disorder mechanism or entropy stabilization. The magnetic properties and the OER performance of these 2D HEHs and the corresponding oxide nanoparticles were preliminarily studied. A reduced overpotential for the OER and superparamagnetism were found in these 2D HEHs and their corresponding oxide nanoparticles, respectively.

Experimental

$Co(NO_3)_2 \cdot 6H_2O$, $CrCl_3 \cdot 6H_2O$, $Mn(NO_3)_2 \cdot 6H_2O$, $Ni(NO_3)_2 \cdot 6H_2O$, and $ZnCl_2$ were purchased from Fujifilm Wako Pure Chemical Co., (Osaka, Japan). Potassium acetate (KOAC, 98.5%), $FeCl_3 \cdot 6H_2O$, ethylene glycol (EG, 99.5%), and sodium hydroxide (NaOH, 10 M aqueous solution) were purchased from Kishida Chemical Co., (Osaka, Japan). All chemicals were analytical grade and used as received. All six metal salts were dissolved in EG and water to give out a 0.2 M solution, denoted as M/EG solution and M/H_2O solution, respectively. KOAC was dissolved in EG to 1.2 M (denoted as KOAC/EG solution). 10 M NaOH aqueous solution was diluted to 1.0 M by using EG (denoted as NaOH/EG solution) or water (denoted as $NaOH/H_2O$ solution). HEHs were synthesized using a simple solvothermal method. Five out of six metal elements were selected to give out six equimolar five-element high-entropy compositions. A seventh composition composed of six metal elements in an equimolar ratio was designed as HEH-7#. Table 1 lists the labels for the HEH compositions regardless of their specific synthesis details. In a typical synthesis procedure, five metal solutions in an equimolar ratio (each 2 mL, 10 mL in total) were mixed with 10 mL KOAC/EG solution (or 5 mL KOAC/EG and 5 mL NaOH/EG) and sealed in an autoclave. The autoclave was heated at 200 °C for 2 h and was then allowed to cool to room temperature naturally. The products were collected by centrifugation, washed with deionized water and ethanol (each 3 times), and dried in a vacuum oven at 50 °C overnight. The dried products were hereafter denoted as synthesized products. EG-K was used to designate the synthesis conditions when M/EG and KOAC/EG solutions were used for solvothermal treatment, while EG-K/N for both KOAC/EG and NaOH/EG solutions was used as a mineralizer. H_2O–K/N indicated that M/H_2O, $KOAC/H_2O$ and $NaOH/H_2O$ solutions were used as starting solutions. The as-synthesized products were annealed in air at temperatures

Table 1 Labels for the seven HEH compositions regardless of their specific synthesis details

Label	Metal elements
HEH-1#	Co, Cr, Fe, Mn, Ni
HEH-2#	Co, Cr, Fe, Mn, Zn
HEH-3#	Co, Cr, Fe, Ni, Zn
HEH-4#	Co, Cr, Mn, Ni, Zn
HEH-5#	Co, Fe, Mn, Ni, Zn
HEH-6#	Cr, Fe, Mn, Ni, Zn
HEH-7#	Co, Cr, Fe, Mn, Ni, Zn

ranging from 200 to 1000 °C for 2 h, respectively. The heating rate was 2 °C min^{-1}.

X-ray diffraction (XRD; Cu-Kα, 30 kV and 10 mA; Bruker D2, Germany) was used to determine the phase assemblage of the samples. The refinement of the powder-XRD patterns was performed using the GSAS software package. XRD patterns used for refinement were collected at 25 °C with 2θ ranging from 5° to 120° and at a scan rate of 0.002° s^{-1}. The metal contents of the samples after 600 °C annealing were measured using an inductively coupled plasma mass spectrometer (ICP-MS, Ultima-2, HORIBA, Japan). The specific surface area of the samples was determined by using a nitrogen adsorption analyzer (Macsorb 1201, MOUNTECH, Japan). The microstructures and elemental distribution of the specimens were analyzed by using a scanning electron microscope (SEM, SU-70, HITACHI, Japan), transmission electron microscope (TEM, JEM 2100F, JEOL, Japan) equipped with an energy-dispersive spectrometer (EDS, Oxford), and atomic force microscope (AFM, NanoNavi S-image, SII, Japan). The pyrolysis behavior of the samples was monitored using a NETZSCH STA 2500 (Germany) in flowing air at temperatures ranging from 40 °C to 800 °C with a heating rate of 10 °C min^{-1}. Fourier transform infrared spectra (FT-IR) were collected using an IRPrestige-21 (Shimadzu, Japan). The pH values of the solutions were measured by using a pH meter (F-52, Horiba, Japan). Magnetic properties were measured by using a superconducting quantum interference device magnetometer (MPMS-XL, Quantum Design, USA).

Electrochemical characterization was carried out using a three-electrode system at 25 °C using an Automatic Polarization System (HZ-3000, Hokuto Denko, Japan). The electrolyte was 0.1 M KOH, the counter electrode was carbon cloth, and the reference electrode was Hg/HgO/0.1 M KOH. 5 mg of sample and 1 mg of carbon black (TKB, TOKABLACK #3855) were dispersed in a mixture of 0.5 mL H_2O, 0.4 mL ethanol, and 0.1 mL Nafion solution (Sigma Aldrich) [equivalent weight (molar mass/mol of ion-exchange sites) = 1100, 5 wt% in a mixture of lower aliphatic alcohols and 15–20% water]. The suspension was ultrasonicated for 30 min to get a homogeneous slurry. The working electrode was prepared by depositing 6 μL slurry onto a glassy carbon electrode with a diameter of 5 mm. Prior to recording cyclic voltammetry data, the working electrode was repeatedly scanned between −0.9 and 0.3 V at 50 mV s^{-1} in an argon atmosphere in order to obtain a stable voltammogram. The linear sweep voltammetry (LSV) curve for the oxygen evolution reaction was recorded in an O_2 atmosphere at 10 mV s^{-1} from 0.2 to 0.8 V. The stability of the catalyst was evaluated by cyclic voltammetry up to 100 cycles. For calculating the current density, the active mass loading was normalized to 1 mg cm^{-2}. The electrode potential ($E_{Hg/HgO}$) was converted to the RHE potential (E_{RHE}) using $E_{(RHE)} = E_{(Hg/HgO)} + 0.177\ V + 0.059 \times pH$.

Results and discussion

Phase composition of the HEHs

Fig. 1 shows the XRD patterns of the as-synthesized products with various compositions after solvothermal treatment at 200 °C for 2 h. All the as-synthesized products demonstrate

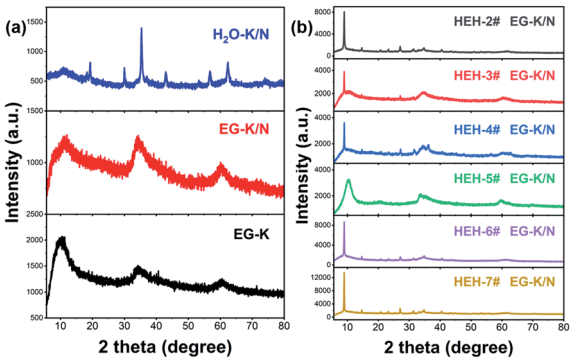

Fig. 1 (a) XRD patterns of the HEH-1# as-synthesized products under H_2O–K/N, EG-K/N, and EG-K synthesis conditions. (b) XRD patterns of HEH-2#–7# as-synthesized products under EG-K/N conditions. All samples were synthesized by solvothermal treatment at 200 °C for 2 h.

a strong low-angle reflection at ~10° and asymmetric diffraction peaks in the high-angle range (Fig. 1 and S1†). These low-angle diffraction peaks can be assigned to interlayer spacing in layered structures, which are described as layers of edge-sharing metal–oxygen octahedra separated by bonded counter ions.[52,54] By using these low-angle reflections, the calculated interlayer distances of the as-synthesized products vary from 0.839 nm to 0.985 nm, as listed in Table 2. Such values are smaller compared with unary polyol-derived metal hydroxides.[54] However, the lack of structural information of these HEHs does not permit their identification by XRD.

ICP-MS was used to determine the chemical compositions for these HEHs. The normalized elemental compositions are gathered in Table 2. ICP-MS results confirm the existence of Co, Cr, Fe, Ni, and Zn elements in a near equimolar ratio for EG-K products. However, the Mn content is much lower than designed, which is probably due to the high solubility of Mn-containing species (Table S1†). The pH of the supernatant after solvothermal treatment is about 8.0 (Table 2), and seldom changes with increasing solvothermal time. The basicity of KOAC is insufficient to precipitate Mn cations completely from multi-component-containing EG solutions, though it has been used to synthesize ternary Mn-containing spinels *via* a similar polyol process.[55] NaOH was used to control the solution pH. Under EG-K/N conditions, whose supernatant pH is 11.5–11.9 (Table 2 and S2†), all HEH-1#–7# EG-K/N as-synthesized products possess similar diffraction patterns compared with EG-K ones, as shown in Fig. 1 and S1.† The calculated interlayer distances of EG-K/N as-synthesized products are slightly larger than the EG-K ones (Table S2†). Taking HEH-1# as an example, an almost perfect equimolar composition can be achieved under these EG-K/N conditions (Table 2). In order to investigate the influence of solvent on the features of the samples, water is used as solvent in HEH-1# cases. In the case of H_2O–K/N, whose supernatant pH is 12.2, a precipitate with five metal species in an equimolar ratio can also be obtained after hydrothermal treatment (Table 2). The H_2O–K/N as-synthesized powders are well crystallized and can be indexed to a spinel structure (Fig. 1a), with the absence of layered structures. The main factor

Table 2 Normalized chemical composition of the 600 °C-annealed products synthesized by solvothermal treatment at 200 °C for 2 h and the pH of the corresponding supernatant after the solvothermal treatment. Calculated interlayer distance for the as-synthesized products

Samples	Chemical composition (at%)						pH	Interlayer distance (nm)
	Co	Cr	Fe	Mn	Ni	Zn		
HEH-1# EG-K	20.3	23.1	24.5	9.3	22.8	—	7.9	0.839
HEH-2# EG-K	21.8	22.8	25.2	7.6	—	22.5	8.0	0.982
HEH-3# EG-K	18.1	21.0	22.5	—	20.2	18.2	8.2	0.985
HEH-4# EG-K	21.3	24.3	—	8.2	24.1	22.0	8.5	0.963
HEH-5# EG-K	21.4	—	24.6	10.0	22.2	21.8	8.4	0.846
HEH-6# EG-K	—	22.9	24.5	8.6	24.6	19.5	8.4	0.850
HEH-1# EG-K/N	20.0	20.4	19.3	20.2	20.1	—	11.5	0.860
HEH-1# H_2O–K/N	19.8	20.5	19.5	19.9	20.3	—	12.2	—

that governs the composition of HEHs in our polyol process at 200 °C is the solution pH. In order to obtain the designed high-entropy composition, it is necessary to carry out the polyol process at a moderate pH that can precipitate the most soluble metal species. It is Mn in our cases. However, higher pH (>13) and/or temperature (>230 °C) will result in the reduction of metal cations during the polyol process, as shown in Fig. S2.†

Morphology and compositional homogeneity of the HEHs

TEM observations combined with elemental mapping were conducted to characterize the morphology and compositional homogeneity of the as-synthesized HEHs. Fig. 2 shows the TEM images on different scales and elemental maps of the HEH-1# as-synthesized products under various conditions. Under EG-K conditions, the as-synthesized products are aggregates of spherical clusters with sizes of about 100–300 nm (Fig. 2a and S3†). These spherical clusters are mainly amorphous, although they contain a few crystallites of ~2 nm in size (Fig. 2b). The elemental mapping of the particles, as shown in Fig. 2c and S3,† indicates the existence of Ni- and Fe-rich clusters on a submicron scale. For Ni-rich clusters, elemental maps at the nanoscale manifest that all five metal elements are homogeneously distributed within clusters, despite their non-equimolar atomic ratios (Fig. S3b and c†). It shows an obvious core–shell like elemental distribution at the nanoscale for Fe-rich clusters (Fig. S3d and e†). In Fe-rich clusters, Fe enriches in the core part and Ni in the shell part, while Co, Cr and Mn elements distribute almost evenly in both parts.

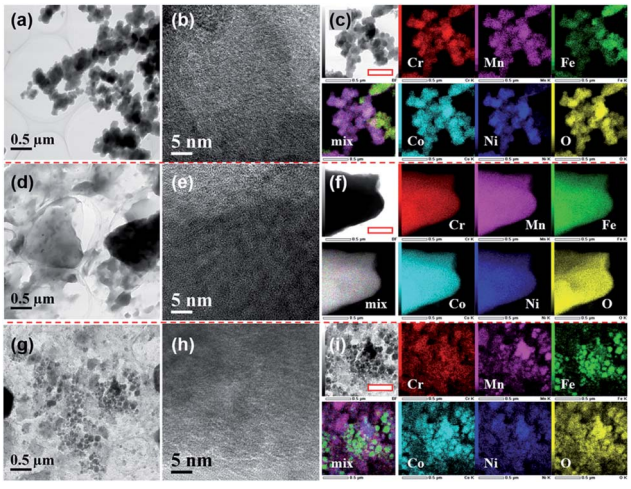

Fig. 2 TEM, HRTEM and EDS maps of the HEH-1# as-synthesized products under different conditions. (a)–(c) EG-K, (d)–(f) EG-K/N, and (g)–(i) H_2O–K/N. Scale bar in (c), (f), and (i) is 0.5 μm. Note: mix figure shows the overlapping Cr, Fe and Ni signals.

Under EG-K/N conditions, in the presence of a moderate amount of OH^- in EG solution, the as-synthesized products present a typical layered morphology, agreeing well with the XRD result, as shown in Fig. 2d and S4a–c.† Fig. 2e shows the HRTEM image of the layered materials, indicating their amorphous structures. All five metal elements are uniformly distributed in the layered structures. No obvious elemental segregation can be observed in the EG-K/N sample at both the submicron and the nanoscale, as shown in Fig. 2f and S4d.† A higher OH^- concentration (*i.e.*, pH) in EG solution will improve the elemental homogeneity compared with the HEH-1# EG-K sample. The AFM image of the HEH-1# EG-K/N as-synthesized sample shows that a thickness of one piece in the sample is about 100 nm (Fig. S4e†). Some irregularly shaped particles are also observed on its surface.

When using water as solvent, the HEH-1# H_2O–K/N as-synthesized powders demonstrate a complicated scenario (Fig. 2g and S5a–c†). Spherical and faceted particles along with large numbers of irregularly shaped particles can be observed. The particle sizes differ greatly from each other. Clear lattice fringes are observed from HRTEM images (Fig. 2h and S5c†), indicating that both the shaped and irregular particles are well crystallized. Elemental mapping results for H_2O–K/N as-synthesized powders (Fig. 2i and S5d†) demonstrate that all five metal element segregation occurs at both the submicron and the nanoscale. By comparing HEH-1# EG-K/N and H_2O–K/N samples, it can be concluded that EG solvent plays a key role in inhibiting elemental segregation.

STEM-EDS quantitative analyses of the HEH-1# as-synthesized products are provided in Fig. 3. In the case of EG-K, both Fe- and Ni-rich clusters are confirmed, as shown in Fig. 3a. The average content values for the five metal elements in the selected area are well consistent with the ICP-MS data. The relative contents of the five metal elements are close to each

other in different particles for Fe- and Ni-rich clusters, respectively. The normalized metal composition is $Cr_{20.7\pm0.7}Mn_{9.9\pm0.5}Fe_{36.2\pm1.7}Co_{22.2\pm0.7}Ni_{11.0\pm0.8}$ and $Cr_{20.9\pm0.4}Mn_{7.4\pm0.1}Fe_{7.6\pm0.3}Co_{23.0\pm0.2}Ni_{41.1\pm0.5}$ for Fe-rich clusters and Ni-rich clusters, respectively. The Ni-rich cluster is probably a compositionally complex single-phase compound, which explains why all five metal elements are homogeneously distributed at the nanoscale (Fig. S3c†). However, the Fe-rich cluster is probably a compositionally complex mixture at the nanoscale, as supported by the obvious Ni segregation shown in Fig. S3e.† In the case of EG-K/N, the EDS quantitative analysis (Fig. 3b) reveals the excellent compositional homogeneity of the layered materials. The five metal cations are in an equimolar ratio at different positions in the layered structures. For H_2O–K/N as-synthesized products, the composition of the particles differs greatly from each other, as shown in Fig. 3c. Each particles contain five metal elements with different stoichiometry, which precipitate separately from solution. The particles share a near equimolar composition on average, agreeing well with the ICP-MS result (Table 2). As aforementioned, two compounds with different stoichiometry (*i.e.*, Fe- and Ni-rich), one compound with the five metal elements in an equimolar ratio, and numbers of spinel-type compounds with various stoichiometry are formed for HEH-1# composition after solvothermal treatment under EG-K, EG-K/N, and H_2O–K/N conditions, respectively. This assumption could facilitate understanding the elemental segregation in the as-synthesized products. Elements should be homogeneously distributed inside one single compound, while elemental separation occurs in compounds with different stoichiometry.

Fig. 4 and S6† compare the microstructure and elemental distribution of the HEH-2#–7# as-synthesized products under EG-K/N and EG-K conditions, respectively. The morphological changes for HEH-2#–7# samples show a similar trend to the HEH-1# ones when increasing the solution pH. For EG-K, the HEH-2#–7#, except for HEH-5#, as-synthesized products generally are aggregates of spherical clusters with elemental segregation at the submicron scale. The most obvious elemental segregation occurs for Ni, Zn, and Fe, as compared in Fig. S6,†

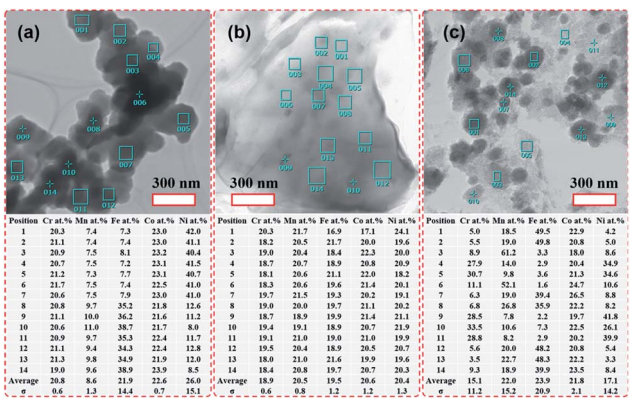

Position	Cr at.%	Mn at.%	Fe at.%	Co at.%	Ni at.%
1	20.3	7.4	7.3	23.0	42.0
2	21.1	7.4	7.4	23.0	41.1
3	20.9	7.5	8.1	23.2	40.4
4	20.7	7.5	7.2	23.1	41.5
5	21.2	7.3	7.7	23.1	40.7
6	21.7	7.5	7.4	22.5	41.0
7	20.6	7.5	7.9	23.0	41.0
8	20.8	9.7	35.2	21.8	12.6
9	21.1	10.0	36.2	21.6	11.2
10	20.6	11.0	38.7	21.7	8.0
11	20.9	9.7	35.3	22.4	11.7
12	21.1	9.4	34.3	22.4	12.8
13	21.3	9.8	34.9	21.9	12.0
14	19.0	9.6	38.9	23.9	8.5
Average	20.8	8.6	21.9	22.6	26.0
σ	0.6	1.3	14.4	0.7	15.1

Position	Cr at.%	Mn at.%	Fe at.%	Co at.%	Ni at.%
1	20.3	21.7	16.9	17.1	24.1
2	18.2	20.5	21.7	20.0	19.6
3	19.0	20.4	18.4	22.3	20.0
4	18.7	20.7	18.9	20.8	20.9
5	18.1	20.6	21.1	22.0	18.2
6	18.3	20.6	19.6	21.4	20.1
7	19.7	21.5	19.3	20.2	19.1
8	19.0	20.0	19.7	21.1	20.2
9	18.7	18.9	19.9	21.4	21.1
10	19.4	19.1	18.9	20.7	21.9
11	19.1	21.0	19.0	21.0	19.9
12	19.5	20.4	18.9	20.5	20.7
13	19.6	18.0	21.0	21.6	19.9
14	18.4	20.8	19.7	20.7	20.3
Average	18.9	20.5	19.5	20.6	20.4
σ	0.6	0.8	1.2	1.2	1.3

Position	Cr at.%	Mn at.%	Fe at.%	Co at.%	Ni at.%
1	5.0	18.5	49.5	22.9	4.2
2	5.5	19.0	49.8	20.8	5.0
3	8.9	61.2	3.3	18.0	8.6
4	27.9	14.0	2.9	20.4	34.9
5	30.7	9.8	3.6	21.3	34.6
6	11.1	52.1	1.6	24.7	10.6
7	6.3	19.0	39.4	26.5	8.8
8	6.8	26.8	35.9	22.2	8.2
9	28.5	7.8	2.2	19.7	41.8
10	33.5	10.6	7.3	22.5	26.1
11	28.8	8.2	2.9	20.2	39.9
12	5.6	20.0	48.2	20.8	5.4
13	3.5	22.7	48.3	22.2	3.3
14	9.3	18.9	39.9	23.5	8.4
Average	15.1	22.0	23.9	21.8	17.1
σ	11.2	15.2	20.9	2.1	14.2

Fig. 3 TEM images of the HEH-1# as-synthesized products under various synthesis conditions and corresponding chemical compositions. (a) EG-K. (b) EG-K/N. (c) H_2O–K/N.

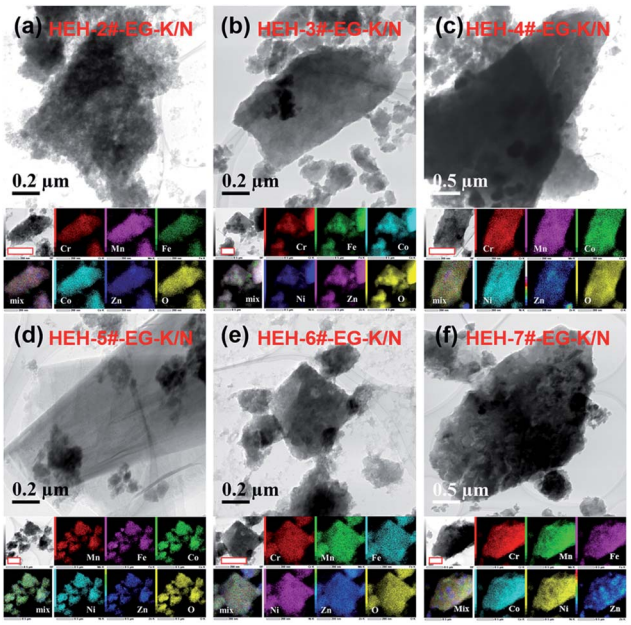

Fig. 4 TEM images and elemental maps for HEH-2#–7# EG-K/N as-synthesized products. Scale bars in the elemental maps are 400 nm.

probably due to the differences in standard electrode potentials and solubility product constants, or a relatively high solvothermal temperature (200 °C).[51] It is worth noting that, for HEH-5# EG-K, the as-synthesized products are aggregates of crumpled nano-sheets with uniform elemental distribution (Fig. S6d†). Increasing the solution pH, the HEH-2#–7# as-synthesized products appear to be layered structures with sizes up to several hundreds of nanometers, as depicted in Fig. 4. These layered materials demonstrate improved elemental homogeneity compared with their corresponding EG-K samples. Taking HEH-5# EG-K/N for an example, all five metal elements are homogeneously distributed in these thin flat sheets, as shown in Fig. 4d and S7.† According to the aforementioned results and discussion, our polyol process is proved to be a simple and effective method for synthesizing layered HEHs with high compositional homogeneity and desired stoichiometry. By simply tuning the solution pH, the morphology of the as-synthesized products can be transformed from the spherical clusters into 2D layered sheets. Some irregularly shaped particles can also be observed in Fig. 4, which warrants further optimization of the synthesis conditions.

FT-IR spectra of the HEHs

Infrared spectroscopy was used to give structural information for these as-synthesized products. FT-IR spectra for HEH-1# samples are illustrated in Fig. 5. EG-K and EG-K/N as-synthesized products have similar spectra, indicating that they probably have similar structures. A broad band at high frequency, centered at 3300 cm^{-1}, can be ascribed to the hydroxyl groups.[53,54,56] Two bands at 2866 cm^{-1} and 2925 cm^{-1} belong to the C–H stretching vibrations.[54] Two intense absorption bands at 1354 cm^{-1} and 1576 cm^{-1} can be assigned to the

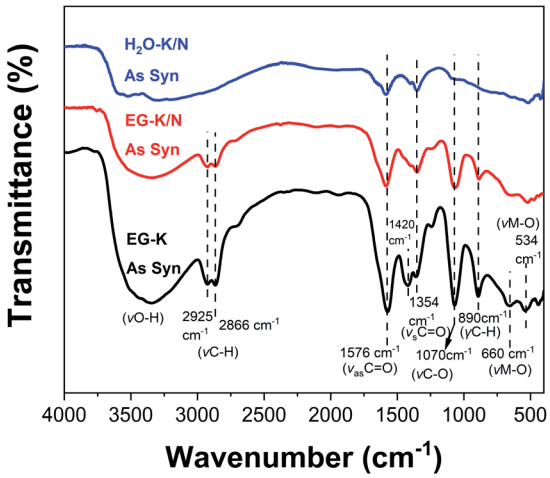

Fig. 5 FT-IR spectra of the HEH-1# as-synthesized products under EG-K, EG-K/N, and H_2O–K/N conditions.

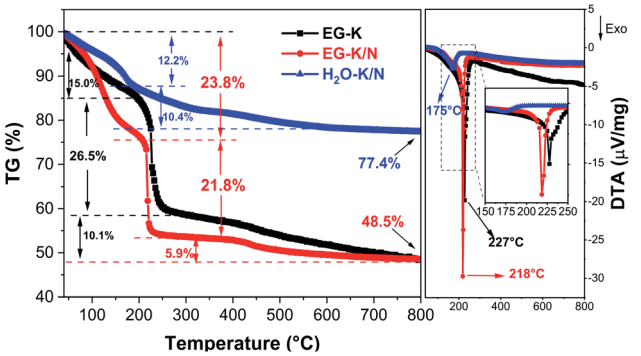

Fig. 6 TG-DTA curves of HEH-1# samples under flowing air.

C═O vibrations.[54,56] A strong absorption band at 1070 cm^{-1} is attributed to the C–O stretching vibration,[53,56] while the band at 890 cm^{-1} is due to the C–H vibration. Lower frequency bands at 660 cm^{-1} and 534 cm^{-1} correspond to metal-O stretching vibrations.[53,54] The C═O, C–O, and C–H groups in EG-K and EG-K/N as-synthesized products must originate from the adsorbed EG or acetate species, or bonded hydrolyzed EG species through metal hydrolysis reactions. The FT-IR spectra of the products synthesized from EG solution indicate the possible formation of metal hydroxide carboxylic compounds, which may be interpreted as $M(OH)_{2-x}\cdot(CH_3COO)_x\cdot nH_2O$ (M stands for Co, Cr, Fe, Mn, and Ni).[54,57] The formation of this organic–inorganic hybrid compound could facilitate co-precipitation of the five metal cations at the nanoscale. For the H_2O–K/N sample, its FT-IR spectrum has medium absorption bands of C═O, C–O, and metal–O. The C═O and C–O in the H_2O–K/N sample probably come from the absorbed or bonded acetate anions during metal hydrolysis.

Thermal evolution of the HEHs

Semiquantitative analysis for the relative content of organic and inorganic components in these as-synthesized products was performed by TG-DTA. Fig. 6 shows the TG-DTA curves of the HEH-1# samples synthesized under EG-K, EG-K/N, and H_2O–K/N conditions. When heated, for H_2O–K/N, the first weight loss (~12.2 wt%) at 40–190 °C associated with a weak exothermic peak centered at 175 °C can be ascribed to the dehydration of the compound and/or release of absorbed water.[54,57] Another 10.4 wt% loss occurs at temperatures above 190 °C probably due to the decomposition of C═O components.[54] It should be noted that the TG curve of H_2O–K/N demonstrates a continuous weight loss in the whole temperature range and no obvious TG plateau is observed. This implies that it possibly has complex components, agreeing well with the TEM and EDS analyses. For EG-K/N as-synthesized products, a first weight loss 23.8 wt% occurs at 40–190 °C (Stage I) and can be ascribed to the removal of intercalated water and dehydroxylation of the layers. A rapid and large weight loss is observed at temperatures ranging from 190 to 240 °C (Stage II) for EG-K/N. This 21.8 wt% loss accompanying by a strong exothermic peak centered at 218 °C in DTA indicates the decomposition of organic groups and release of gaseous products (*e.g.*, H_2O, CO or CO_2).[54] A TG plateau is observed at temperatures between 240 °C and 400 °C. Another 6 wt% loss occurs at temperatures above 400 °C to 800 °C (Stage III), which possibly correspond to the further decomposition of the compound. The residue is 48.5 wt% and 77.4 wt% for EG-K/N and H_2O–K/N as-synthesized products, respectively. Such a residue difference supports the assumption that EG participates in metal hydrolysis reactions.[51,54] The EG-K sample possesses typical three weight loss stages similar to the EG-K/N sample. The dehydration and organic decomposition weight losses are 15.0 wt% and 26.5 wt%, which are smaller and larger than those for the EG-K/N sample, respectively. A continuous weight loss of 10.1 wt% is observed at temperatures 300–800 °C. Such a weight loss difference indicates that the EG-K/N sample contains more OH^- and less organic content compared with the EG-K sample. TG-DTA and FT-IR analyses confirm the formation of high-entropy inorganic–organic hybrid compounds, possibly metal hydroxide acetates, during solvothermal reactions. Assuming that the weight loss in Stage I is ascribed to the removal of OH^- and H_2O and the weight loss in Stage II is ascribed to the decomposition of acetate groups, the estimated formula for the compound synthesized under EG-K/N and EG-K conditions is $M(OH)_{1.41}\cdot(CH_3COO)_{0.59}\cdot0.78H_2O$ and $M(OH)_{1.28}\cdot(CH_3COO)_{0.72}\cdot0.12H_2O$, respectively.[54,56]

A relatively high solution pH makes it possible to precipitate all metal cations completely with targeted composition (on average) from solution. Meanwhile, the polyol solvent plays a key role in inhibiting elemental segregation possibly through forming polyol-based metal hydroxides.[50,51] It has been reported that reduction and hydrolysis are the main chemical reactions during the polyol process.[51] The existence of OH^- and acetate ions can facilitate the complexation of polyol with metal cations through deprotonating the hydroxyl group.[51] A higher pH results in increased OH^- and H_2O contents in the as-synthesized HEHs. More OH^- and H_2O in the compound may facilitate stabilizing the layers composed of edge-sharing metal–oxygen octahedra and thus benefit the formation of 2D layered sheets through the polyol process.[54]

The phase evolution and morphological change of the annealed particles are investigated by XRD and TEM-EDS. Fig. 7 shows the XRD patterns of the HEH-1# EG-K/N as-synthesized products before and after annealing at 200–600 °C. The low-angle diffraction peak disappears after annealing at 200 °C, confirming the decomposition of the metal hydroxide. For HEH-2#–7# EG-K/N as-synthesized products, low-angle reflections disappear upon annealing, indicating the collapse of M–OH lamellar structures, as shown in Fig. S8a.† The crystallinity of the nanoparticles increases with increasing annealing temperature. It demonstrates a well crystallized spinel-type structure after annealing at 600 °C, as compared in Fig. 7 and S8b.† Rietveld fitting of 600 °C-annealed HEH-1# EG-K/N nanoparticles (Fig. S9†) gives a unit cell lattice parameter of 8.3128 Å and volume of 574.457 Å^3. The crystallite size calculated by using the Scherrer equation is 12.6 nm for HEH-1# EG-K/N.[58]

Fig. 8 shows the TEM images and elemental maps for HEH-1# EG-K/N nanoparticles after annealed in air at 200 and 600 °C. The 2D layered morphology is well maintained after 200 °C annealing. Thin, flat and large-area layers of HEMs composed of nanoparticles can be clearly observed in Fig. 8a and b. The HRTEM image in Fig. 8c shows that the crystallites are about 5 nm in size and have high crystallinity. They possess the same lattice plane that can be indexed to the (311) plane of the spinel structure. Fig. 8d clearly shows that all metal elements are uniformly distributed without any obvious segregation. The specific surface area of the 200 °C-annealed nanoparticles is 242.0 m^2 g^{-1}. These results manifest that 2D layered high-entropy spinel oxides can be successfully synthesized through our polyol process, followed by post-annealing treatment at 200 °C, a low synthesis temperature compared with other methods.[33,36,59–61] The flat nanosheets become a particulate when annealed at 600 °C. The size of the nanoparticles

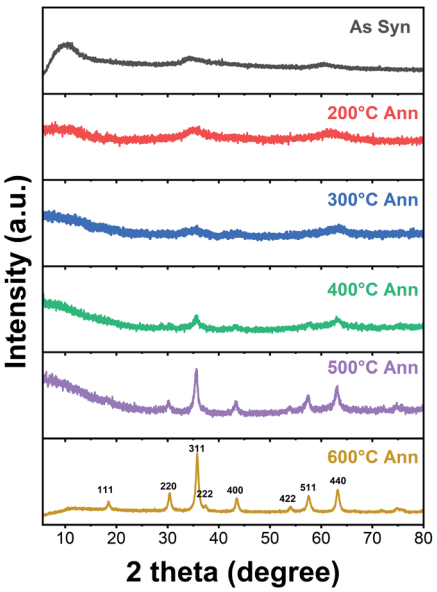

Fig. 7 XRD patterns of HEH-1# EG-K/N as-synthesized products before and after annealing in air at 200–600 °C for 2 h, respectively.

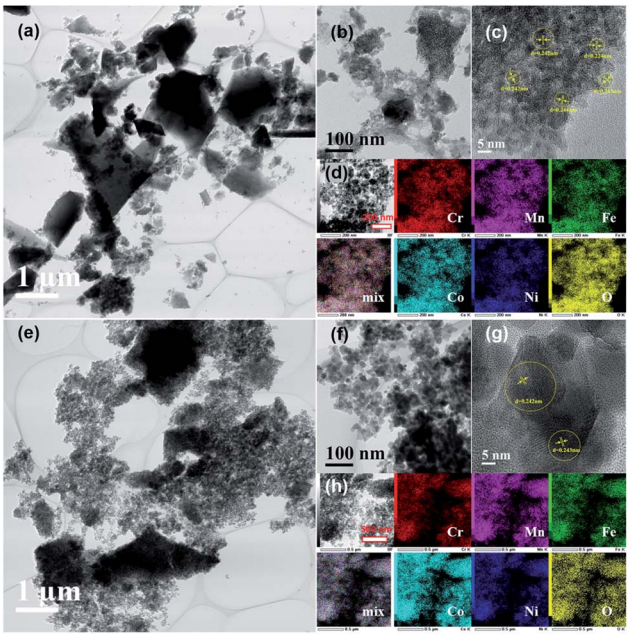

Fig. 8 TEM images with different magnifications and elemental maps for the HEH-1# EG-K/N sample after annealed at (a)–(d) 200 °C and (e)–(h) 600 °C.

increases (Fig. 8e–g), and the specific surface area decreases to 49.5 m^2 g^{-1}. In Fig. 8g, clear lattice fringes can be observed, which can also be indexed to the (311) plane of the spinel structure. All five metal elements are well distributed on the nanoparticles. For HEH-1# EG-K and H_2O–K/N as-synthesized products, their phase evolution upon heating is similar to the EG-K/N sample. Increasing the annealing temperature only leads to the increased crystallinity of the nanoparticles (Fig. S10†). After annealing at 600 °C, their XRD patterns can be indexed to a single-phase spinel structure of high crystallinity. However, they should be indeed mixtures of spinel particles with various compositions, as evidenced by the TEM-EDS analyses in Fig. S11.†

Magnetic property of the HEHs and corresponding spinel nanoparticles

Fig. 9 illustrates the zero field-cooled (ZFC) and field cooled (FC) magnetization curves for the HEH-1# EG-K/N as-synthesized and 600 °C-annealed nanoparticles recorded at a magnetic field of 100 Oe. The ZFC and FC curves for HEH-1# EG-K/N samples after 1000 °C annealing treatment are also provided for comparison. Fig. 10 shows the field dependent magnetization curves (*M*–*H* curves) for the HEH-1# as-synthesized and the annealed nanoparticles at 2 K and 300 K.

The FC curve of the as-synthesized sample shows a steady decrease to near zero in the whole measuring temperature range, while a weak anomaly is indicated where the ZFC curve shows the maximum, indicating that the magnetic transition is around 5 K. The corresponding M–H curve shows a ferromagnetic hysteresis loop at 2 K. However, it is not magnetically saturated even at 50 × 10^3 Oe, suggesting that ferromagnetism

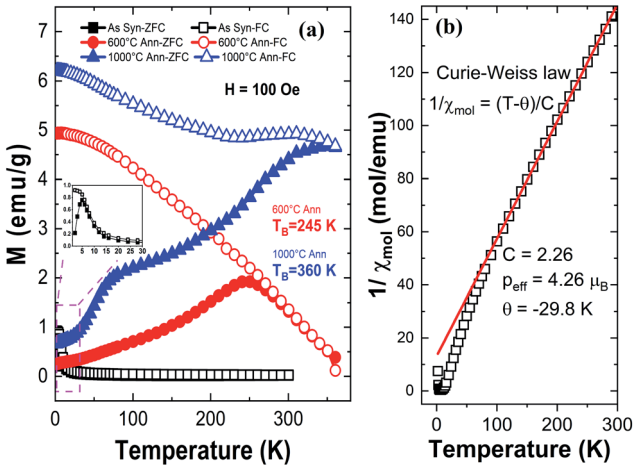

Fig. 9 (a) Temperature dependence of magnetic susceptibility of HEH-1# EG-K/N as-synthesized and annealed nanoparticles measured after Zero-Field Cooling (ZFC) and Field Cooling (FC) with magnetic fields of 100 Oe. (b) A fit of the Curie–Weiss law to the ZFC curve of the HEH-1# EG-K/N as-synthesized sample. *C*: Curie constant, θ: Weiss temperature and P_{eff}: effective paramagnetic moment.

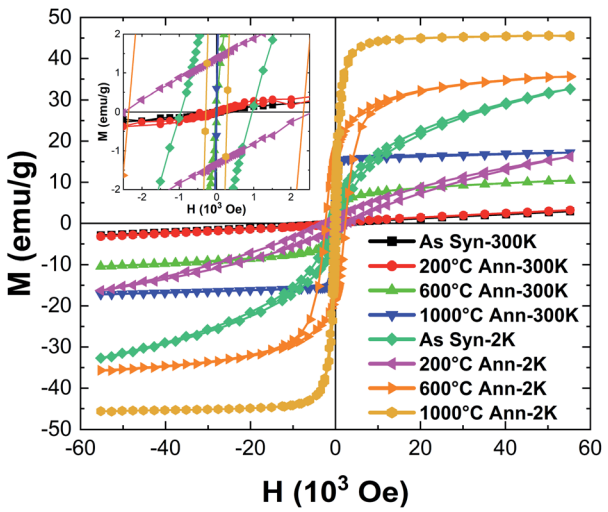

Fig. 10 Magnetization curves *vs.* magnetic field (*M*–*H* curves) for HEH-1# EG-K/N as-synthesized and annealed nanoparticles recorded at 300 K and 2 K. The inset shows the expanded view of the *M*–*H* curves.

and paramagnetism coexist. On the other hand, at high temperatures, the temperature dependence of magnetization (Fig. 9a) and the M–H curve (Fig. 10) indicate that it is paramagnetic. In fact, above about 100 K, the magnetization obeyed the Curie–Weiss law with negative Weiss temperature (θ) (Fig. 9b). The negative Weiss temperature indicates antiferromagnetic interaction between magnetic ions. The magnetic properties observed in the as-synthesized samples at low temperatures may be due to the presence of multiple magnetic ions coupled antiferromagnetically with neighbouring magnetic ones having different magnetic moments.[62]

The ZFC and FC curves for the 600 °C-annealed nanoparticles are more magnetized than those for the as-synthesized sample. They are also similar to those of ZFC-FC observed for superparamagnetic nanoparticles;[63] the ZFC curve exhibits a peak, indicating a transition from a magnetically blocked state (low temperature) to a superparamagnetic state (high temperature). As can be seen from Fig. 9a, the blocking temperature (T_B) for 600 °C-annealed nanoparticles is estimated to be 245 K. For particles annealed at 1000 °C, the ZFC curve indicates a fast increase at 2–75 K and increase with a relatively slow rate above 75 K, and eventually overlaps the FC curve at temperature above ~360 K. Assuming the overlapping point as the maximum of the ZFC curve, the T_B would be ~360 K. The crystallite size of the 1000 °C-annealed particles is 40.5 nm calculated by using the Scherrer equation, which is larger than that of the 600 °C-annealed one. The blocking temperature increases as the volume of the particle increases, agreeing well with previous publications.[63] The shapes of the ZFC curves could be explained by a magnetic anisotropy of magnetic domains and the inter-site exchange interactions among different metal cations at different sublattices.[64,65] It requires further study to get a better understanding of the composition-metal species-magnetic property relationship, which is beyond the scope of this work.

The *M*–*H* curves recorded at 300 K represent superparamagnetic behavior, agreeing well with the ZFC-FC plots, with inappreciable coercivity and residual magnetization, as compared in Table 3 and Fig. S12.† The saturation magnetization (M_s) increases as the annealing temperature (*i.e.*, the crystallite size) increases. It becomes comparable to that of the control sample prepared by solid state reactions when annealed at 1000 °C. The M–H plots recorded at 2 K demonstrate hysteresis loops for both the as-synthesized and annealed nanoparticles. It is interesting to note that the coercivity decreases dramatically from 2339.0 Oe to 284.3 Oe, while the residual magnetization and saturation magnetization decreases from 17.5 emu g^{-1} to 9.5 emu g^{-1} and increases from 30.8 emu g^{-1} to 44.5 emu g^{-1} for 600 °C- and 1000 °C-annealed nanoparticles, respectively. The coercivity for the 1000 °C-annealed sample at 300 K and 2 K does not change so much, while that of the other samples increases dramatically with the reduction of temperature. The ZFC-FC and M–H plots confirm a very strong dependence of the magnetic properties on the annealing temperature, which is correlated with the increased crystallite size and crystallinity of the samples.

OER performance of the HEHs

OER studies were preliminarily performed on HEH-1# and 5# compositions. Fig. 11 shows the LSV polarization curves of HEH-1# and 5# as-synthesized products under EG-K and EG-K/N conditions. The annealed samples and carbon black are also provided for comparison. Typical OER behaviors are recorded for our materials.[38,49,66,67] The HEH-5# (CoFeMnNiZn–OH) composition demonstrates better OER performance than the HEH-1# (CoCrFeMnNi–OH) composition both under EG-K and EG-K/N synthesis conditions. It has been reported that the OER performance could be tuned by modulating the 3d electronic

Table 3 Coercivity (H_c), residual magnetization (M_r) and saturation magnetization (M_s) of HEH-1# EG-K/N as-synthesized and annealed nanoparticles

Sample	Temperature (K)	Coercivity H_c (Oe)	Residual magnetization M_r (emu g^{-1})	Saturation magnetization M_s (emu g^{-1})
As syn	2	961.0	3.7	17.6
200 °C ann	2	2532.5	1.4	4.9
600 °C ann	2	2339.0	17.5	30.8
1000 °C ann	2	284.3	9.5	44.5
As syn	300	0.0	0.0	0.2
200 °C ann	300	38.5	0.0	0.5
600 °C ann	300	15.4	0.3	7.7
1000 °C ann	300	104.5	0.6	16.0
Control[a]	2	565.0	16.0	43.1
Control[a]	300	70.4	3.3	16.3

[a] Note: Control sample was prepared by solid state reactions using Co, Cr, Fe, Mn, and Ni binary oxides as raw materials at 1000 °C for 1 h.

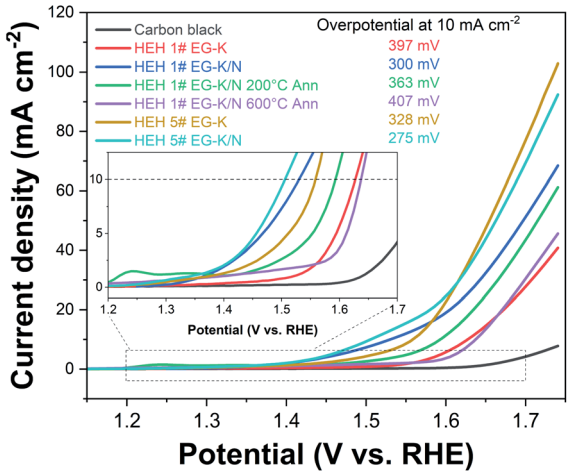

Fig. 11 LSV curves of the HEH-1# and 5# as-synthesized products under various conditions, HEH-1# EG-K/N 200 °C- and 600 °C-annealed nanoparticles, and carbon black. Inset shows the expanded view for these curves.

structure of the catalyst.[68] In our materials, the substitution of Cr with Zn largely improves the OER performance. For both HEH-1# and 5# compositions, the EG-K/N as-synthesized products outperform their corresponding EG-K samples. The calculated interlayer space of HEH-1# and 5# EG-K/N as-synthesized products is 0.860 nm and 0.863 nm, while that for the corresponding EG-K product is 0.839 nm and 0.846 nm, respectively. Expanding the interlayer space of these layered hydroxides will enhance OER performance, which agrees well with previous reports.[38,49] A relatively low Mn content in EG-K as-synthesized samples may be another reason for their reduced OER performance (Table 2). The HEH-5# EG-K/N as-synthesized sample shows the best OER performance among our materials and requires an overpotential of only 275 mV at 10 mA cm^{-2} and a low onset potential. A unique 2D layered structure with defects and the multi-element synergistic effect may be the main factors responsible for its excellent OER performance.[38,49,67] Annealing these 2D HEHs leads to the reduction of their OER activity, possibly due to the collapse of layered structures and increase of crystallinity.[49] For HEH-1# EG-K/N samples, the as-synthesized 2D HEM requires an overpotential of 300 mV to reach a current density of 10 mA cm^{-2}, while that for the 200 °C- and 600 °C-annealed samples is 363 mV and 407 mV, respectively. Generally speaking, all our polyol-derived HEHs outperform or at least are comparable to previously reported high-entropy oxides or hydroxides, such as (FeCrCoNiCu)–OH nanosheets (330 mV at 10 mA cm^{-2}),[42] (CoCrFeMnNi)-glycerate microspheres (229 mV at 10 mA cm^{-2}),[49] $(CoCuFeMnNi)_3O_4$ nanoparticles (400 mV at 10 mA cm^{-2}),[32] $(MgCoNiCu)_{0.6}Fe_{0.4}$–O nanoparticles (300 mV at 10 mA cm^{-2}),[69] CoCuFeMoOH nanosheets on Cu foil (199 mV at 10 mA cm^{-2}),[70] and nanoporous ultra-high-entropy alloys (274 mV at 10 mA cm^{-2}),[71] although different OER testing parameters were used. These preliminary results indicate that the catalytic activity of the polyol-derived HEHs is strongly compositionally oriented and microstructure dependent. These findings may provide further avenues to optimize their catalytic performance. The OER stability was evaluated by cyclic voltammetry up to 100 cycles, as shown in Fig. S13.† An activation process during the initial 10 cycles was observed. After the 100th LSV cycle, the catalyst showed almost the same OER activity, verifying its good stability.

Conclusions

In summary, 2D layered high-entropy transition metal hydroxides are successfully synthesized *via* a simple and feasible bottom-up polyol process. The polyol approach involves the dissolution, hydrolysis, and condensation of multiple metal cations in ethylene glycol media along with a moderate amount of OH^-. High temperature (>230 °C) or pH (>13) should be avoided in order to suppress the reduction of metal cations by reducing ethylene glycol. The homogeneous distribution of the multiple metal cations of equimolar stoichiometry can be achieved by performing the polyol process under mild conditions, *e.g.*, 200 °C and pH of ~11.5 in this work. The as-synthesized transition metal hydroxides show an obvious 2D layered morphology with interlayer distances ranging from 0.860 to 0.987 nm. These 2D HEHs demonstrate promising

electrochemical catalytic activity for the OER, exhibiting a low overpotential of 275 mV (at 10 mA cm^{-2}) for (CoFeMnNiZn)–OH. When annealed at 200 °C, the 2D HEHs are converted to spinel-type high-entropy nanoparticles with a size of 5 nm and specific surface area of 242.0 m^2 g^{-1}. The resultant spinel-type nanoparticles are superparamagnetic at room temperature. Our work opens the door for synthesizing low-dimensional functional high-entropy materials (*e.g.*, spinel, pyrochlore, fluorite and perovskite oxides, and layered double hydroxides) through a feasible bottom-up soft chemistry method.

Author contributions

Fei Li and Hiroya Abe: conceptualization, methodology, and writing – original draft. Shi-Kuan Sun, Yinjuan Chen, Takashi Naka, Takeshi Hashishin, and Jun Maruyama: methodology. All the authors contributed to the discussion and review & editing of the paper.

Conflicts of interest

There are no conflicts to declare.

Acknowledgements

The authors would like to thank Dr Sadahiro Yagishita from Daiichi Kigenso Kagaku Kogyo Co., Ltd for ICP-MS and nitrogen adsorption measurement. This study is supported by JSPS KAKENHI Grant Number 21H01637 for Basic Research: Category B, and the Project to Create Research and Educational Hubs for Innovative Manufacturing in Asia, Osaka University, funded by the Special Budget Project of the Ministry of Education, Culture, Sports, Science and Technology.

References

1 B. Cantor, I. T. H. Chang, P. Knight and A. J. B. Vincent, *Mater. Sci. Eng., A*, 2004, **375–377**, 213–218.
2 J. W. Yeh, S. K. Chen, S. J. Lin, J. Y. Gan, T. S. Chin, T. T. Shun, C. H. Tsau and S. Y. Chang, *Adv. Eng. Mater.*, 2004, **6**, 299–303.
3 C. M. Rost, E. Sachet, T. Borman, A. Moballegh, E. C. Dickey, D. Hou, J. L. Jones, S. Curtarolo and J.-P. Maria, *Nat. Commun.*, 2015, **6**, 8485.
4 E. P. George, D. Raabe and R. O. Ritchie, *Nat. Rev. Mater.*, 2019, **4**, 515–534.
5 C. Oses, C. Toher and S. Curtarolo, *Nat. Rev. Mater.*, 2020, **5**, 295–309.
6 N. Dragoe and D. Bérardan, *Science*, 2019, **366**, 573–574.
7 Y. Sun and S. Dai, *Sci. Adv.*, 2021, **7**, eabg1600.
8 F. Li, L. Zhou, J.-X. Liu, Y. Liang and G.-J. Zhang, *J. Adv. Ceram.*, 2019, **8**, 576–582.
9 Y. Qin, J.-X. Liu, F. Li, X. Wei, H. Wu and G.-J. Zhang, *J. Adv. Ceram.*, 2019, **8**, 148–152.
10 H. Li, H. Zhu, S. Zhang, N. Zhang, M. Du and Y. Chai, *Small Struct.*, 2020, **1**, 2000033.
11 Y. J. Ma, Y. Ma, Q. S. Wang, S. Schweidler, M. Botros, T. T. Fu, H. Hahn, T. Brezesinski and B. Breitung, *Energy Environ. Sci.*, 2021, **14**, 2883–2905.
12 W.-T. Koo, J. E. Millstone, P. S. Weiss and I.-D. Kim, *ACS Nano*, 2020, **14**, 6407–6413.
13 A. Sarkar, Q. Wang, A. Schiele, M. R. Chellali, S. S. Bhattacharya, D. Wang, T. Brezesinski, H. Hahn, L. Velasco and B. Breitung, *Adv. Mater.*, 2019, **31**, e1806236.
14 T. Li, Y. Yao, Z. Huang, P. Xie, Z. Liu, M. Yang, J. Gao, K. Zeng, A. H. Brozena, G. Pastel, M. Jiao, Q. Dong, J. Dai, S. Li, H. Zong, M. Chi, J. Luo, Y. Mo, G. Wang, C. Wang, R. Shahbazian-Yassar and L. Hu, *Nat. Catal.*, 2021, **4**, 62–70.
15 J. X. Yang, B.-H. Dai, C.-Y. Chiang, I. C. Chiu, C.-W. Pao, S.-Y. Lu, I. Y. Tsao, S.-T. Lin, C.-T. Chiu, J.-W. Yeh, P.-C. Chang and W.-H. Hung, *ACS Nano*, 2021, **15**, 12324–12333.
16 Y. Wang, T. Csanádi, H. Zhang, J. Dusza, M. J. Reece and R.-Z. Zhang, *Adv. Theory Simul.*, 2020, **3**, 2000111.
17 T. J. Harrington, J. Gild, P. Sarker, C. Toher, C. M. Rost, O. F. Dippo, C. McElfresh, K. Kaufmann, E. Marin, L. Borowski, P. E. Hopkins, J. Luo, S. Curtarolo, D. W. Brenner and K. S. Vecchio, *Acta Mater.*, 2019, **166**, 271–280.
18 P. Sarker, T. Harrington, C. Toher, C. Oses, M. Samiee, J.-P. Maria, D. W. Brenner, K. S. Vecchio and S. Curtarolo, *Nat. Commun.*, 2018, **9**, 4980.
19 J. Gild, Y. Zhang, T. Harrington, S. Jiang, T. Hu, M. C. Quinn, W. M. Mellor, N. Zhou, K. Vecchio and J. Luo, *Sci. Rep.*, 2016, **6**, 37946.
20 J.-X. Liu, X.-Q. Shen, Y. Wu, F. Li, Y. Liang and G.-J. Zhang, *J. Adv. Ceram.*, 2020, **9**, 503–510.
21 M. D. Qin, Q. Z. Yan, Y. Liu and J. Luo, *J. Adv. Ceram.*, 2021, **10**, 166–172.
22 T. Jin, X. Sang, R. R. Unocic, R. T. Kinch, X. Liu, J. Hu, H. Liu and S. Dai, *Adv. Mater.*, 2018, **30**, 1707512.
23 X. Q. Chen and Y. Q. Wu, *J. Am. Ceram. Soc.*, 2020, **103**, 750–756.
24 J. Gild, J. Braun, K. Kaufmann, E. Marin, T. Harrington, P. Hopkins, K. Vecchio and J. Luo, *J. Materiomics*, 2019, **5**, 337–343.
25 R.-Z. Zhang and M. J. Reece, *J. Mater. Chem. A*, 2019, **7**, 22148–22162.
26 M. M. Liu, Z. H. Zhang, F. Okejiri, S. Z. Yang, S. H. Zhou and S. Dai, *Adv. Mater. Interfaces*, 2019, **6**, 1900015.
27 D. Wu, K. Kusada, T. Yamamoto, T. Toriyama, S. Matsumura, I. Gueye, O. Seo, J. Kim, S. Hiroi, O. Sakata, S. Kawaguchi, Y. Kubota and H. Kitagawa, *Chem. Sci.*, 2020, **11**, 12731–12736.
28 F. Li, Y. Lu, X.-G. Wang, W. Bao, J.-X. Liu, F. Xu and G.-J. Zhang, *Ceram. Int.*, 2019, **45**, 22437–22441.
29 D. Wu, K. Kusada, T. Yamamoto, T. Toriyama, S. Matsumura, S. Kawaguchi, Y. Kubota and H. Kitagawa, *J. Am. Chem. Soc.*, 2020, **142**, 13833–13838.
30 Y. Yao, Z. Huang, P. Xie, S. D. Lacey, R. J. Jacob, H. Xie, F. Chen, A. Nie, T. Pu, M. Rehwoldt, D. Yu, M. R. Zachariah, C. Wang, R. Shahbazian-Yassar, J. Li and L. Hu, *Science*, 2018, **359**, 1489–1494.

31 T. Li, Y. Yao, B. H. Ko, Z. Huang, Q. Dong, J. Gao, W. Chen, J. Li, S. Li, X. Wang, R. Shahbazian-Yassar, F. Jiao and L. Hu, *Adv. Funct. Mater.*, 2021, **31**, 2010561.
32 D. Wang, Z. Liu, S. Du, Y. Zhang, H. Li, Z. Xiao, W. Chen, R. Chen, Y. Wang, Y. Zou and S. Wang, *J. Mater. Chem. A*, 2019, **7**, 24211–24216.
33 T. X. Nguyen, J. Patra, J.-K. Chang and J.-M. Ting, *J. Mater. Chem. A*, 2020, **8**, 18963–18973.
34 C. R. McCormick and R. E. Schaak, *J. Am. Chem. Soc.*, 2021, **143**, 1017–1023.
35 T. Wang, H. Chen, Z. Yang, J. Liang and S. Dai, *J. Am. Chem. Soc.*, 2020, **142**, 4550–4554.
36 G. Wang, J. Qin, Y. Feng, B. Feng, S. Yang, Z. Wang, Y. Zhao and J. Wei, *ACS Appl. Mater. Interfaces*, 2020, **12**, 45155–45164.
37 K. S. Novoselov, A. K. Geim, S. V. Morozov, D. Jiang, Y. Zhang, S. V. Dubonos, I. V. Grigorieva and A. A. Firsov, *Science*, 2004, **306**, 666–669.
38 L. Lv, Z. Yang, K. Chen, C. Wang and Y. Xiong, *Adv. Energy Mater.*, 2019, **9**, 1803358.
39 H. Zhang, *ACS Nano*, 2015, **9**, 9451–9469.
40 C. Tan, X. Cao, X.-J. Wu, Q. He, J. Yang, X. Zhang, J. Chen, W. Zhao, S. Han, G.-H. Nam, M. Sindoro and H. Zhang, *Chem. Rev.*, 2017, **117**, 6225–6331.
41 Y.-N. Zhou, R.-Y. Fan, Y.-N. Cao, H.-Y. Wang, B. Dong, H.-Y. Zhao, F.-L. Wang, J.-F. Yu and Y.-M. Chai, *Nanoscale*, 2021, **13**, 13463–13472.
42 K. Gu, X. Zhu, D. Wang, N. Zhang, G. Huang, W. Li, P. Long, J. Tian, Y. Zou, Y. Wang, R. Chen and S. Wang, *J. Energy Chem.*, 2021, **60**, 121–126.
43 K. Gu, D. Wang, C. Xie, T. Wang, G. Huang, Y. Liu, Y. Zou, L. Tao and S. Wang, *Angew. Chem., Int. Ed. Engl.*, 2021, **60**, 20253–20258.
44 S. K. Nemani, B. Zhang, B. C. Wyatt, Z. D. Hood, S. Manna, R. Khaledialidusti, W. Hong, M. G. Sternberg, S. K. R. S. Sankaranarayanan and B. Anasori, *ACS Nano*, 2021, **15**, 12815–12825.
45 Z. Du, C. Wu, Y. Chen, Z. Cao, R. Hu, Y. Zhang, J. Gu, Y. Cui, H. Chen, Y. Shi, J. Shang, B. Li and S. Yang, *Adv. Mater.*, 2021, **33**, e2101473.
46 T. Ying, T. Yu, Y.-S. Shiah, C. Li, J. Li, Y. Qi and H. Hosono, *J. Am. Chem. Soc.*, 2021, **143**, 7042–7049.
47 J. Cavin, A. Ahmadiparidari, L. Majidi, A. S. Thind, S. N. Misal, A. Prajapati, Z. Hemmat, S. Rastegar, A. Beukelman, M. R. Singh, K. A. Unocic, A. Salehi-Khojin and R. Mishra, *Adv. Mater.*, 2021, **33**, e2100347.
48 A. Miura, S. Ishiyama, D. Kubo, N. C. Rosero-Navarro and K. Tadanaga, *J. Ceram. Soc. Jpn.*, 2020, **128**, 336–339.
49 T. X. Nguyen, Y.-H. Su, C.-C. Lin, J. Ruan and J.-M. Ting, *Adv. Sci.*, 2021, **8**, 2002446.
50 H. Dong, Y. C. Chen and C. Feldmann, *Green Chem.*, 2015, **17**, 4107–4132.
51 F. Fiévet, S. Ammar-Merah, R. Brayner, F. Chau, M. Giraud, F. Mammeri, J. Peron, J. Y. Piquemal, L. Sicard and G. Viau, *Chem. Soc. Rev.*, 2018, **47**, 5187–5233.
52 G. Fan, F. Li, D. G. Evans and X. Duan, *Chem. Soc. Rev.*, 2014, **43**, 7040–7066.
53 M. Wang, J. Jiang and L. Ai, *ACS Sustainable Chem. Eng.*, 2018, **6**, 6117–6125.
54 L. Poul, N. Jouini and F. Fiévet, *Chem. Mater.*, 2000, **12**, 3123–3132.
55 H. Deng, X. Li, Q. Peng, X. Wang, J. Chen and Y. Li, *Angew. Chem., Int. Ed.*, 2005, **44**, 2782–2785.
56 T. Fan, D. Pan and H. Zhang, *Ind. Eng. Chem. Res.*, 2011, **50**, 9009–9018.
57 D. Larcher, G. Sudant, R. Patrice and J. M. Tarascon, *Chem. Mater.*, 2003, **15**, 3543–3551.
58 U. Holzwarth and N. Gibson, *Nat. Nanotechnol.*, 2011, **6**, 534.
59 A. Mao, H.-Z. Xiang, Z.-G. Zhang, K. Kuramoto, H. Zhang and Y. Jia, *J. Magn. Magn. Mater.*, 2020, **497**, 165884.
60 J. Dąbrowa, M. Stygar, A. Mikuła, A. Knapik, K. Mroczka, W. Tejchman, M. Danielewski and M. Martin, *Mater. Lett.*, 2018, **216**, 32–36.
61 M. Stygar, J. Dąbrowa, M. Moździerz, M. Zajusz, W. Skubida, K. Mroczka, K. Berent, K. Świerczek and M. Danielewski, *J. Eur. Ceram. Soc.*, 2020, **40**, 1644–1650.
62 A. Sarkar, B. Eggert, R. Witte, J. Lill, L. Velasco, Q. Wang, J. Sonar, K. Ollefs, S. S. Bhattacharya, R. A. Brand, H. Wende, F. M. F. de Groot, O. Clemens, H. Hahn and R. Kruk, *Acta Mater.*, 2022, **226**, 117581.
63 G. C. Papaefthymiou, *Nano Today*, 2009, **4**, 438–447.
64 A. Sarkar, R. Kruk and H. Hahn, *Dalton Trans.*, 2021, **50**, 1973–1982.
65 J. Cieslak, M. Reissner, K. Berent, J. Dabrowa, M. Stygar, M. Mozdzierz and M. Zajusz, *Acta Mater.*, 2021, **206**, 116600.
66 W. Wang, J. Luo and S. Chen, *Chem. Commun.*, 2017, **53**, 11556–11559.
67 J. Maruyama, S. Maruyama, T. Fukuhara, Y. Takao and K. Miyazaki, *Eur. J. Inorg. Chem.*, 2019, **2019**, 4117–4121.
68 B. Zhang, X. Zheng, O. Voznyy, R. Comin, M. Bajdich, M. García-Melchor, L. Han, J. Xu, M. Liu, L. Zheng, F. P. G. d. Arquer, C. T. Dinh, F. Fan, M. Yuan, E. Yassitepe, N. Chen, T. Regier, P. Liu, Y. Li, P. D. Luna, A. Janmohamed, H. L. Xin, H. Yang, A. Vojvodic and E. H. Sargent, *Science*, 2016, **352**, 333–337.
69 T. X. Nguyen, Z.-T. Huang and J.-M. Ting, *Appl. Surf. Sci.*, 2021, **570**, 151160.
70 L. Zhang, W. Cai and N. Bao, *Adv. Mater.*, 2021, **33**, 2100745.
71 Z.-X. Cai, H. Goou, Y. Ito, T. Tokunaga, M. Miyauchi, H. Abe and T. Fujita, *Chem. Sci.*, 2021, **12**, 11306–11315.